



Nondegenerate parametric oscillations in a tunable superconducting resonator

Downloaded from: <https://research.chalmers.se>, 2023-05-05 03:11 UTC

Citation for the original published paper (version of record):

Bengtsson, A., Krantz, P., Simoen, M. et al (2018). Nondegenerate parametric oscillations in a tunable superconducting resonator. *Physical Review B*, 97(14).
<http://dx.doi.org/10.1103/PhysRevB.97.144502>

N.B. When citing this work, cite the original published paper.

Nondegenerate parametric oscillations in a tunable superconducting resonator

Andreas Bengtsson,^{1,*} Philip Krantz,² Michaël Simoen,¹ Ida-Maria Svensson,¹ Ben Schneider,¹ Vitaly Shumeiko,¹ Per Delsing,¹ and Jonas Bylander¹

¹*Microtechnology and Nanoscience, Chalmers University of Technology, SE-412 96, Göteborg, Sweden*

²*Research Laboratory of Electronics, Massachusetts Institute of Technology, Cambridge, Massachusetts 02139, USA*



(Received 14 January 2018; published 4 April 2018)

We investigate nondegenerate parametric oscillations in a superconducting microwave multimode resonator that is terminated by a superconducting quantum interference device (SQUID). The parametric effect is achieved by modulating magnetic flux through the SQUID at a frequency close to the sum of two resonator-mode frequencies. For modulation amplitudes exceeding an instability threshold, self-sustained oscillations are observed in both modes. The amplitudes of these oscillations show good quantitative agreement with a theoretical model. The oscillation phases are found to be correlated and exhibit strong fluctuations which broaden the oscillation spectral linewidths. These linewidths are significantly reduced by applying a weak on-resonant tone, which also suppresses the phase fluctuations. When the weak tone is detuned, we observe synchronization of the oscillation frequency with the frequency of the input. For the detuned input, we also observe an emergence of three idlers in the output. This observation is in agreement with theory indicating four-mode amplification and squeezing of a coherent input.

DOI: [10.1103/PhysRevB.97.144502](https://doi.org/10.1103/PhysRevB.97.144502)

I. INTRODUCTION

The circuit quantum electrodynamics architecture (cQED) [1,2] is an attractive platform for quantum information processing with continuous variables. Within cQED, a variety of nonclassical photonic states can be efficiently generated by nonlinear superconducting elements: superpositions of Fock states [3], entangled two-mode photonic states [4–6], and multiphoton Schrödinger cat states [7]. Parametric phenomena have played important roles in this development.

A typical cQED parametric device consists of a high-quality superconducting resonator integrated with Josephson elements that induce a Kerr nonlinearity in the resonator and also allow for rapid modulation of the resonator frequency [8–11].

By means of such a modulation at a frequency twice the resonator-mode frequency, a degenerate Josephson parametric oscillator (JPO) regime is achieved [12]. The JPO regime is established at parametric pump amplitudes above a critical value (threshold), where an instability of the resonator ground state is developed, and it is stabilized by the Kerr nonlinearity. The JPO can be used for vacuum squeezing and photonic entanglement [13,14], photonic qubit operation [15], and cat-state engineering [16–18]. The JPO has also been employed for high-fidelity readout of superconducting qubits [19,20].

In this paper, we report on an experimental investigation of a different regime, the nondegenerate Josephson parametric oscillator (NJPO). In this regime, self-sustained oscillations of two resonator modes, n and m , are excited by modulating the Josephson inductance at a frequency close to the sum of the mode frequencies, $\omega_p \approx \omega_n + \omega_m$. A detailed theory of nondegenerate parametric resonance was developed in Ref. [21].

Some properties of the nondegenerate parametric resonance in the subthreshold region, amplification [6,22] and frequency conversion [23,24], have been experimentally investigated.

Our interest in the NJPO is driven by potentially novel, compared to the JPO, quantum statistical properties of the generated field. The novelty is related to the presence of additional idlers and multimode squeezing [21] and large phase fluctuations resulting from a continuous degeneracy of the oscillator state. The latter is analogous to an extensively studied effect in optical parametric oscillators [25–33]. Similar parametric oscillations were recently observed and investigated in a mechanical resonator [34]. To date, neither classical nor quantum properties of the NJPO have been experimentally verified. The aim of this work is to fill this gap. We investigate the quasiclassical dynamics of the NJPO: intensity and frequency of the oscillations as functions of the pump parameters, properties of the phase dynamics, and response to external coherent inputs.

II. EXPERIMENTAL METHODS

The investigated device is a coplanar waveguide resonator, capacitively coupled to a transmission line at one end and shorted to ground via a dc superconducting quantum interference device (SQUID) at the other end [see Fig. 1(a)]. The resonator is reactive-ion etched from a sputtered thin-film of niobium on a high-resistivity silicon substrate. The SQUID is deposited with a two-angle evaporation of aluminum. The layout of the device is similar to that in Ref. [22]. The distance between the interdigitated coupling capacitor and the SQUID is 31 nm, yielding a fundamental resonant frequency $\omega_1/2\pi = 912$ MHz. The available measurement frequency window is 4–8 GHz, limited by the microwave setup, giving experimental access to the higher resonator modes with numbers 3, 4, and 5.

*andreas.bengtsson@chalmers.se

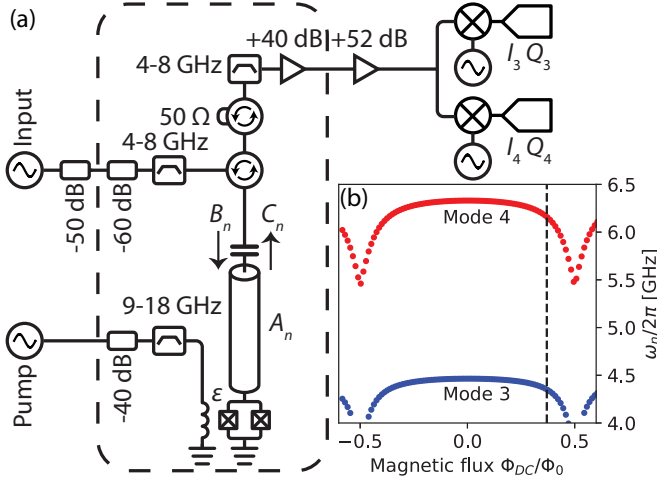


FIG. 1. (a) Schematic of the experimental setup, where the dashed box indicates the dilution refrigerator. The device consists of a capacitively coupled resonator shorted to ground via a SQUID. The magnetic flux through the SQUID is modulated, with an effective amplitude ϵ , via an on-chip microwave line. There are three types of fields present in the system: in-resonator fields A_n , input fields B_n , and outgoing fields C_n , where the latter two are separated by a microwave circulator. The outgoing fields are amplified and split into two vector digitizers measuring the quadratures I_n and Q_n . (b) Measured resonant frequencies for modes 3 (blue) and 4 (red) as a function of magnetic flux through the SQUID loop. The vertical dashed line marks the static flux bias, $\Phi_{DC} = 0.37\Phi_0$, used here to generate nondegenerate parametric oscillations.

A setup schematic is shown in Fig. 1(a). The device is mounted at the mixing chamber of a dilution refrigerator with a base temperature of 10 mK.

The magnetic field through the SQUID loop can be applied statically via an external coil or modulated via an on-chip flux line. The resonant frequencies for modes 3 and 4, as functions of the static magnetic flux Φ_{DC} , are shown in Fig. 1(b).

Each mode of the NJPO is characterized by the resonant frequency ω_n , external loss rate Γ_{n0} , total loss rate Γ_n , and Kerr coefficient α_n . The resonant frequencies and loss rates are determined by data fitting of measured complex reflection coefficients. At the static flux bias $\Phi_{DC} = 0.37\Phi_0$, indicated in Fig. 1(b), we find $\omega_3/2\pi = 4.345$ GHz, $\omega_4/2\pi = 6.150$ GHz, $\Gamma_{30}/2\pi = 0.52$ MHz, $\Gamma_3/2\pi = 0.56$ MHz, $\Gamma_{40}/2\pi = 0.70$ MHz, and $\Gamma_4/2\pi = 0.78$ MHz. The Kerr coefficients are determined from properties of the parametric oscillations and explained later.

A microwave signal generator supplies the coherent pump tone to the on-chip, inductively coupled flux line via an attenuated and filtered coaxial cable. The output of the resonator is routed through microwave filters and two circulators to a cryogenic low-noise amplifier. The output is further amplified at room temperature before detection. Additionally, to investigate the system response, an input field can be applied to the resonator via the first circulator.

The quadrature voltages of the output are acquired by heterodyne detection. Two sets of digitizers, mixers, and local oscillators allow for a simultaneous detection of two

modes far separated in frequency. From each digitizer, we transfer the digitally down-converted quadrature voltages to a computer for further processing. The output power from each mode P_n is calculated and related to the output photon flux $|C_n|^2$, $|C_n|^2 = (P_n - P_{\text{noise}})/(G\hbar\omega_d)$, where P_{noise} is the system noise power measured with the pump off and ω_d is the detection frequency. In a similar way, the quadrature voltages are converted to dimensionless quantities, $I_n(t)$ and $Q_n(t)$, corresponding to the square root of the number of photons per second and unit bandwidth. The system gain G is calibrated at each mode frequency using a shot-noise tunnel junction (SNTJ) connected to a microwave switch at the mixing chamber of the refrigerator [35]. The SNTJ is a normal-insulator-normal-tunnel junction, which, when current biased, generates a known amount of shot noise. By sweeping the current bias while measuring the output power, the gain can be extracted via the derivative of the measured power with respect to the bias current.

III. RESULTS

A. Parametric oscillations

We excite the parametric resonance by modulating the SQUID inductance at a frequency close to the sum of the frequencies of modes 3 and 4, $\omega_p = \omega_3 + \omega_4 + 2\delta$, where δ refers to the pump detuning. The quantum resonant two-mode dynamics is generally described with a Hamiltonian written in a doubly rotating frame with frequencies $\omega_{3,4} + \delta$ [13,21],

$$H/\hbar = - \sum_{n=3,4} [\delta a_n^\dagger a_n + (\alpha_n/2)(a_n^\dagger a_n)^2] - 2\alpha(a_3^\dagger a_3 a_4^\dagger a_4) - \epsilon(a_3 a_4 + a_3^\dagger a_4^\dagger), \quad (1)$$

where a_n is the annihilation operator of the in-resonator field of mode n , ϵ is the effective amplitude of the parametric pump, and $\alpha = \sqrt{\alpha_3 \alpha_4}$ is the cross-Kerr coefficient.

Throughout this work, we restrict our interpretation of experimental data to a quasiclassical model of the resonator dynamics, which, instead of operators, has classical field amplitudes $A_n(t)$. The amplitudes satisfy two dynamical equations,

$$i\dot{A}_3 + (\zeta_3 + i\Gamma_3)A_3 + \epsilon A_4^* = \sqrt{2\Gamma_{30}}B_3(t), \\ i\dot{A}_4 + (\zeta_4 + i\Gamma_4)A_4 + \epsilon A_3^* = \sqrt{2\Gamma_{40}}B_4(t), \quad (2)$$

where $B_n(t)$ is an external driving field and ζ_n is a nonlinear detuning including the Kerr-induced frequency shifts,

$$\zeta_3 = \delta + \alpha_3|A_3|^2 + 2\alpha|A_4|^2, \\ \zeta_4 = \delta + \alpha_4|A_4|^2 + 2\alpha|A_3|^2. \quad (3)$$

The normalization of the field amplitudes is such that $|A_n|^2$ and $|B_n|^2$ correspond to the number of photons in mode n and the incoming photon flux, respectively. Parametric self-sustained oscillations correspond to nontrivial solutions of the homogeneous nonlinear equations (2) and (3).

1. Parametric instability

By ramping the pump amplitude we observe a strong increase in the output photon flux above a certain pump threshold,

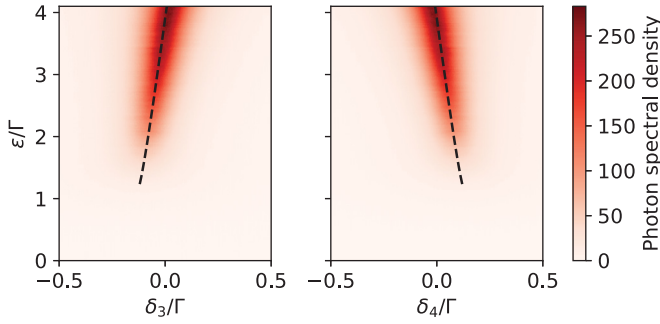


FIG. 2. Parametric instability. Measured photon spectral densities of the output from modes 3 (left) and 4 (right). The parametric pump has an amplitude ϵ and is applied at a detuning $\delta = 0.26\Gamma$. The detection frequency detunings δ_n are relative to each respective rotating frame. The dashed lines are the radiation frequencies from Eq. (5).

as shown in Fig. 2. The radiation is detected at a frequency ω_d , associated with the excited resonator modes but deviating from the respective rotating frame, $\delta_n = \omega_d - (\omega_n + \delta)$, in good agreement with a theoretical prediction [21],

$$\delta_3 = -\delta_4 = \delta \frac{\Gamma_3 - \Gamma_4}{\Gamma_3 + \Gamma_4}. \quad (4)$$

With a further increase of the pump power, the radiation frequencies shift, as shown in Fig. 2. This shift is accurately described by the equation [21]

$$\delta_3(\epsilon) = -\delta_4(\epsilon) = \Delta_0 = \frac{\Gamma_3\zeta_4 - \Gamma_4\zeta_3}{\Gamma_3 + \Gamma_4}. \quad (5)$$

The instability of the resonator ground state occurs within an interval of the pump detuning,

$$|\delta| < \delta_{th}(\epsilon) = \frac{\Gamma_3 + \Gamma_4}{2} \sqrt{\frac{\epsilon^2}{\Gamma^2} - 1}. \quad (6)$$

This criterion defines three regions in the ϵ - δ plane, as presented in Fig. 3:

- (I) At $\epsilon < \Gamma$ or $\delta > \delta_{th}(\epsilon)$ only the ground state, $A_n = 0$, is stable.
- (II) At $\epsilon > \Gamma$ and $|\delta| < \delta_{th}(\epsilon)$ the ground state is unstable, and self-sustained oscillations emerge.
- (III) At $\epsilon > \Gamma$ and $\delta < -\delta_{th}(\epsilon)$ the ground state regains stability, while the self-sustained oscillations persist; this is a bistability region.

2. Output intensities

A quantitative analysis of the intensity of the oscillations is performed by solving Eq. (2),

$$|A_3|^2 = \frac{2\Gamma_4(\delta_{th}(\epsilon) - \delta)}{\alpha_3\Gamma_4 + \alpha_4\Gamma_3 + 2\alpha(\Gamma_3 + \Gamma_4)}, \quad (7)$$

$$|A_4|^2 = \frac{\Gamma_3}{\Gamma_4} |A_3|^2. \quad (8)$$

The output intensity is given by the relation $|C_n|^2 = 2\Gamma_{n0}|A_n|^2$; for the experimentally extracted external and total losses, $|C_3|^2 \approx |C_4|^2$.

The measured output intensities are shown in Figs. 3(a) and 3(b), while the computed intensities of the oscillations

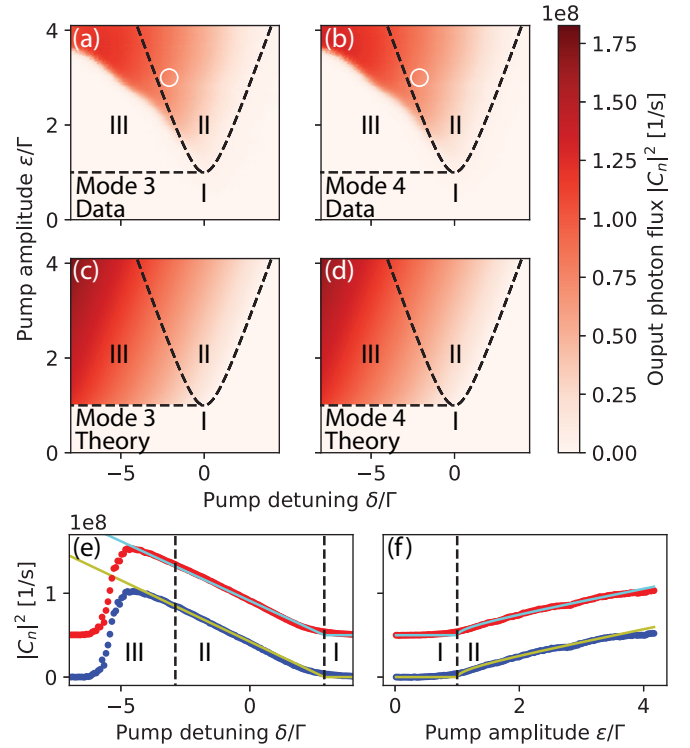


FIG. 3. Nondegenerate pumping of modes $n = 3$ and 4 at the frequency $\omega_p = \omega_3 + \omega_4 + 2\delta$. (a) and (b) Experimentally measured and (c) and (d) theoretically calculated output intensities $|C_n|^2$ vs pump detuning δ and amplitude ϵ . I–III indicate the three different stability regions described in the main text. (e) Horizontal line cuts of (a)–(d) at $\epsilon = 3\Gamma$. (f) Vertical line cuts of (a)–(d) at $\delta = 0$. In (e) and (f) the dots are measured values, and solid lines are calculated from theory. The data and the theory for mode 4 are offset in the positive y direction for clarity.

are shown in Figs. 3(c) and 3(d). The output intensities as a function of the pump detuning at a fixed pump amplitude $\epsilon = 3\Gamma$ are presented in Fig. 3(e). The data and the theory are in excellent agreement in region II and down to $\delta \approx -4.5\Gamma$ in region III, implying that the system is mostly in the excited state up to this point. Below $\delta \approx -4.5\Gamma$, the measured output intensities decrease, indicating a system preference to occupy the ground state. Figure 3(f) illustrates the growth of the output intensities with the pump amplitude at $\delta = 0$, also showing good agreement with the theory.

The slope of the output intensity with respect to δ in Fig. 3(e) defines a relation between the Kerr coefficients; a second relation is given by the coefficient of the linear dependence of the oscillation frequency in Eq. (5) versus the oscillation intensity. Fitting the data in Figs. 2 and 3(e) with Eqs. (5) to (8) yields the values $\alpha_3/2\pi = 71$ KHz and $\alpha_4/2\pi = 178$ KHz. Furthermore, the data in Fig. 3(f) are in good agreement with Eqs. (6) and (7), which allows us to establish a scaling between the amplitude of the signal applied to the flux line and ϵ . This scaling is also consistent with the data in Fig. 2.

3. Phase dynamics

We further investigate the phase properties of the parametric oscillations. To this end, we choose the point in

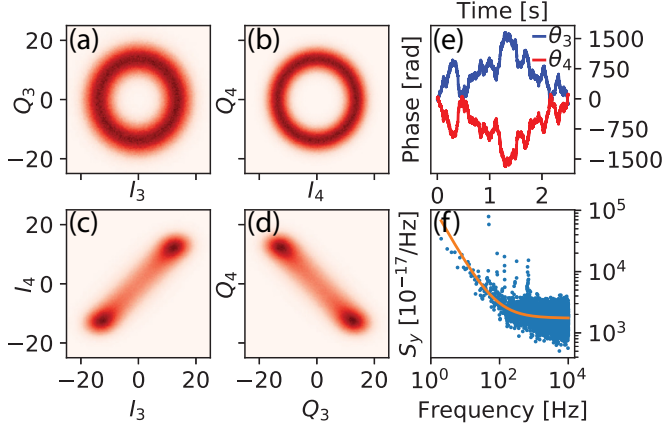


FIG. 4. Phase-space distributions for nondegenerate parametric oscillations measured at the point indicated by the white circles in Fig. 2. (a) and (b) The distributions for modes 3 and 4. The color scale is proportional to the number of counts in each bin. (c) and (d) Two out of four cross-quadrature histograms, showing clear anticorrelation between the mode phases θ_n . (e) Evolution of the phases θ_n in time. (f) Spectrum of the fractional frequency fluctuations S_y of the parametric oscillations in mode 3. The solid line shows a combination of $1/f$ and white noise.

the δ - ϵ space indicated by the white circles in Figs. 3(a) and 3(b) and acquire 1 million samples for the quadratures $I_n(t)$ and $Q_n(t)$ during 2.5 s of measurement time. By creating two-dimensional histograms, we present the data in Figs. 4(a) and 4(b). The oscillations have a finite average amplitude, while the phase is evenly distributed between $-\pi$ and π . This observation supports the theoretical prediction about a continuous degeneracy of the oscillator state with respect to the phase [21]. More precisely, the oscillator phases $|A_n|e^{i\theta_n}$ respect the constraint

$$\begin{aligned} \theta_3 + \theta_4 &= \Theta, \quad \Theta \in \{\pi/2, \pi\}, \\ \tan \Theta &= -\frac{1}{\sqrt{\epsilon^2/\Gamma^2 - 1}}, \end{aligned} \quad (9)$$

while the difference of the phases, $\psi = \theta_3 - \theta_4$, is arbitrary. Such a degeneracy gives rise to phase diffusion under the effect of vacuum fluctuations, which underlines the broadening of the spectrum of the output signal in Fig. 2.

To reveal the intermode phase correlation, we synchronize the digitizers by using a common trigger. This allows us to create the cross-quadrature histograms I_3, I_4 and Q_3, Q_4 in a way analogous to the phase-space distributions. Figures 4(c) and 4(d) present the cross-quadrature histograms for quadratures chosen such that their common output phase Θ is compensated by the phases of the local oscillators. With such a choice, the histograms exhibit the relations $I_3 = I_4$ and $Q_3 = -Q_4$. To further illustrate the phase anticorrelation property, we plot in Fig. 4(e) a time-evolution realization of the phases of the two modes. A similar behavior was observed in a mechanical resonator with a dominant Kerr nonlinearity [34].

The effective frequency-noise spectrum can be extracted from the phase evolution. It is presented for mode 3 in Fig. 4(f). The spectrum is in good agreement with a $1/f$ component combined with white noise. The origin of the low-frequency

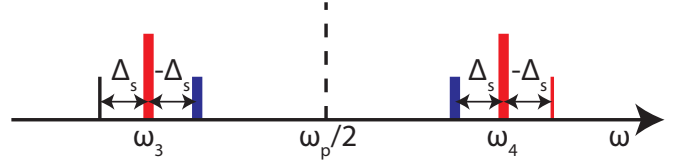


FIG. 5. Frequency diagram of the four-mode amplification. The dashed line is the parametric pump, the thick red lines are the parametric oscillations, the thin black line is the coherent signal, the thin red line is the primary idler, and the thick blue lines are the secondary idlers.

noise is most likely due to flux noise through the SQUID loop, which is known to have a $1/f$ spectrum [36].

B. Response to an external signal

In this section, we explore the response of the NJPO to an external coherent input. The linear response of parametric systems to weak external signals exposes many properties of quantum noise. For instance, the presence of an idler in parametric amplification below the parametric instability threshold defines the structure of a squeezed vacuum and two-mode entanglement of the output photons [4–6]. This is true for both degenerate and nondegenerate parametric resonances, with the only difference being that for the nondegenerate case, the idler has a frequency far detuned from the signal frequency and appears within the bandwidth of the conjugated mode [22], while for the degenerate case, the idler appears within the bandwidth of the signal mode.

Above the threshold, the situation is qualitatively similar for the JPO [13]. However, for the NJPO, the situation is quite different. Here, the strong fields produced by the parametric oscillations in the two resonator modes generate, through a four-mode mixing mechanism, two additional idlers [21] (see Fig. 5). The intensities of these secondary idlers are proportional to the oscillation intensities $|A_n|^2$, while the intensity of the primary idler is defined by, and proportional to, the flux pump intensity ϵ^2 . This process of four-mode amplification should result in four-mode quantum noise squeezing. The output noise should also be influenced by the strong fluctuations of the oscillation phases discussed above.

In this section, we present data that corroborate the presence of the three idlers in the NJPO response. In addition, we observe two effects that imply a strong influence of the input signal on the oscillator phase dynamics: phase locking and frequency synchronization.

1. Injection locking

It is generally known that in self-sustained oscillators possessing phase degeneracy, large phase fluctuations can be suppressed by injecting a small, but frequency stable, signal in resonance with the oscillator [37]. This effect is explained by a violation of the symmetry of the phase degeneracy by external driving. The phase-locking effect has been observed in a nondegenerate optical parametric oscillator [38]. For our system, it has been shown [21] that applying an input with the same frequency as the oscillator frequency locks the oscillator

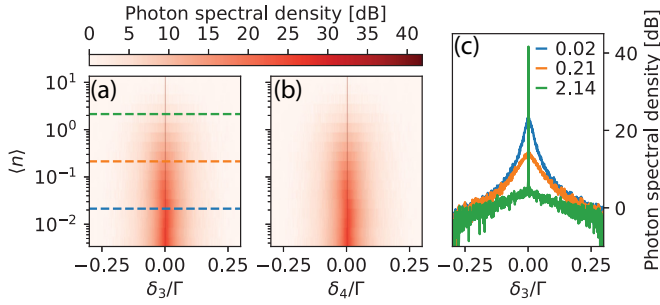


FIG. 6. Photon spectral densities of a nondegenerate parametric oscillator under injection locking. The scale is presented in a logarithmic unit relative to 1 photon/(s Hz). (a) and (b) The output radiation for modes 3 and 4, respectively. δ_n is the detuning between the detection frequency and the center frequency of the radiation in the respective mode, and $\langle n \rangle$ is the average input photon number for mode 3. (c) Line cuts of (a) at the three input photon numbers indicated by the corresponding colored dashed lines in (a).

phase to the value defined by the phase of the input θ_{in} ,

$$\theta_3 = \theta_{in} - \arctan \frac{3\Gamma}{2\sqrt{\epsilon^2 - \Gamma^2}}. \quad (10)$$

Due to the intermode phase coupling, Eq. (9), both modes are phase locked simultaneously.

We investigate this locking effect by injecting a coherent signal B_3 in resonance with the parametric oscillations in mode 3. We characterize the input field with an average number of coherent photons $\langle n \rangle = |B_3|^2 / (2\Gamma_{30})$. To quantify the efficiency of the injection locking, we measure the output spectral densities as functions of $\langle n \rangle$, which is presented in Figs. 6(a) and 6(b). In Fig. 6(c), we plot line cuts for mode 3 for several values of $\langle n \rangle$. For low input photon numbers, the radiation line is still broad, but when the input power is increased, the width is substantially reduced, and if it is increased further, the frequency noise is removed almost entirely. The -3 dB point is below the resolution bandwidth of 1 Hz, implying a frequency noise reduction of at least a factor of 5000. This narrowing effect becomes pronounced at $\langle n \rangle \geq 0.5$, similar to the level that was found to phase lock the JPO [19]. This result can be understood from the following argument: under the effect of vacuum noise, the oscillator phase undergoes random motion, which is shown in Fig. 4(f) as the white frequency noise above 100 Hz. This random motion can be constrained only by a coherent input intensity exceeding that of the vacuum fluctuations, $\langle n \rangle = 1/2$.

Figures 7(a)–7(f) illustrate the phase-space distributions for both modes at the same input powers as in Fig. 6(c). The calculated phase distributions and standard deviations are presented in Figs. 7(g) and 7(h), respectively, as functions of the input photon number. The phase distribution is uniform between $-\pi$ and π for small injection signals and has a standard deviation close to that expected for a uniform distribution: $\pi/\sqrt{3}$. For increasing $\langle n \rangle$, the distribution approaches a Gaussian form, and the standard deviation saturates. It is difficult to compare the eventually locked phase with the theoretical value, Eq. (10), because of the difficulty of experimentally calibrating the precise phase accumulation between the resonator and the detectors.

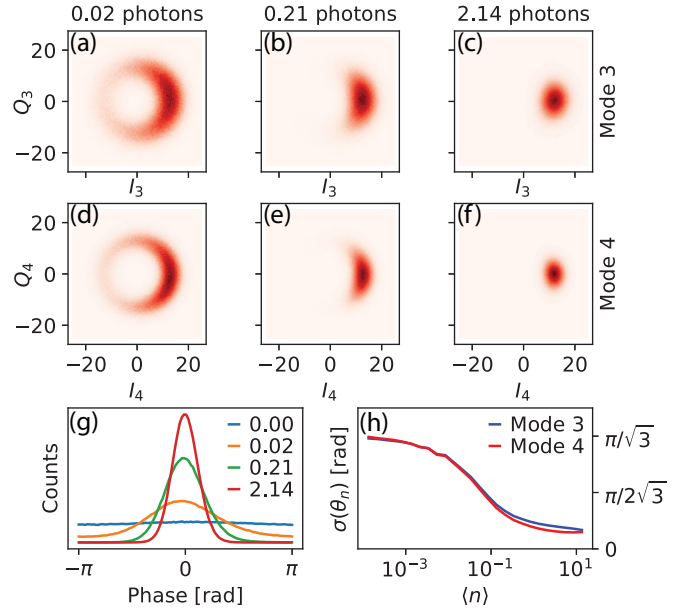


FIG. 7. Phase locking of nondegenerate parametric oscillations by signal injection. Phase-space histograms for the parametric radiation in modes (a)–(c) 3 and (d)–(f) 4, with a coherent signal injected into mode 3. The input photon numbers $\langle n \rangle$ are indicated above each column and are the same as in Fig. 6(c). The color scale is proportional to the number of counts in each bin. (g) Distributions of the phase θ_3 of the parametric oscillations in mode 3 for different input photon numbers. (h) Standard deviation of the phases θ_n as a function of the input photon number for mode 3.

2. Synchronization and secondary idlers

Applying an input signal detuned from the oscillation frequency gives rise to the interesting and related phenomenon of frequency synchronization [37,39]. We introduce a detuning Δ_s between the injection signal and the parametric oscillations in mode 3 and study the output photon spectral densities of both modes as functions of Δ_s and $\langle n \rangle$ [see Figs. 8(a)–8(d)]. Within a certain interval of detuning, we observe a sudden change in the oscillation frequency, which synchronizes with the frequency of the input. Simultaneously, the frequency of the conjugated mode synchronizes with the frequency of the primary idler. Due to the dramatic decrease of the linewidth of the synchronized output signal, the effect appears in Figs. 8(a)–8(d) as a gap in frequency space where the oscillations have the same frequency as the locking signal. The gap size is proportional to the size of the synchronization detuning window, which in turn is proportional to the square root of the input power [37]. In Fig. 8(e), we quantify the gap size and find good agreement with the predicted square-root dependence.

Figures 8(a)–8(d) also reveal the presence of three idlers in the output. The output signal in mode 3, seen as a thin diagonal line in Figs. 8(a) and 8(c) [hardly visible at the small intensity in Fig. 8(a)], generates a primary idler in mode 4, seen as a thin diagonal line in the opposite direction compared to the signal in Figs. 8(b) and 8(d). This idler has its frequency detuned by $-\Delta_s$ from the oscillation frequency in this mode, and it has a small linewidth, similar to the signal. The two secondary idlers are

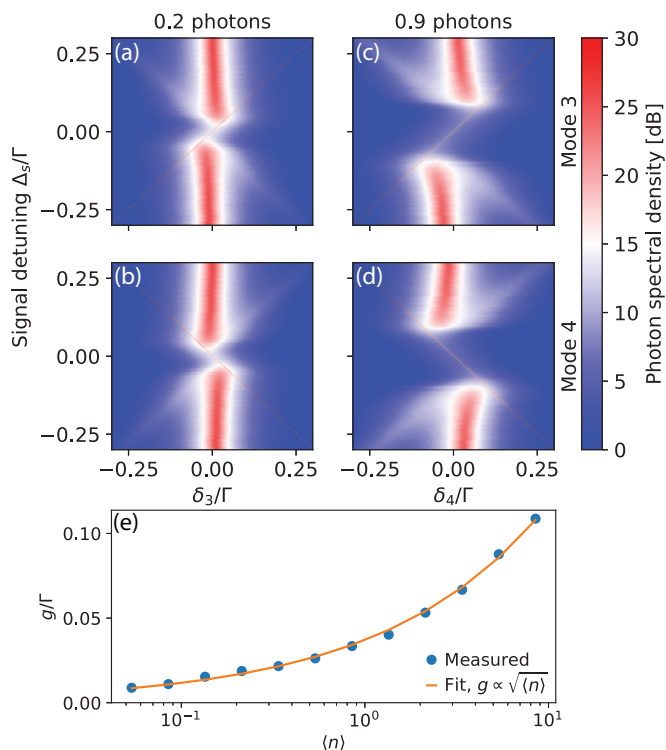


FIG. 8. Response of the parametric oscillations to a detuned signal. (a)–(d) The output photon spectral densities on a logarithmic scale for (a) and (c) mode 3 and (b) and (d) mode 4. The detection detunings δ_n are relative to the center of the parametric oscillations in the respective mode. The signal detuning Δ_s is the detuning between the coherent signal and the center of the oscillation frequency in mode 3. The input photon number is indicated above each column. (e) The obtained size of the frequency gap g and a fit to $g \propto \sqrt{\langle n \rangle}$.

visible in Figs. 8(a) to 8(d). The secondary idler in Figs. 8(a) and 8(c) is detuned by $-\Delta_s$ from the oscillation frequency of mode 3, while the secondary idler in Figs. 8(b) and 8(d) is detuned by Δ_s from the oscillation frequency of mode 4. These

secondary idlers are generated by the in-resonator fields of the parametric oscillator, and they are much broader than the signal and primary idler; their linewidths are instead comparable to those of the oscillations.

IV. CONCLUSION

In conclusion, we investigated a nondegenerate Josephson parametric oscillator using a tunable superconducting resonator. By modulating the magnetic flux through the SQUID, which is attached to the resonator, we generated intense correlated output radiation of two resonator modes. The measured radiation frequencies and intensities as functions of the pump parameters show excellent quantitative agreement with theory. A correlated phase dynamics of the oscillations was directly observed, and a continuous phase degeneracy of the oscillations was demonstrated. We also demonstrated significant suppression of the phase fluctuations when a weak, on-resonant coherent signal was applied: the oscillation linewidths were reduced by at least three orders of magnitude. In addition, a frequency synchronization effect was observed when the input signal was detuned from the resonance. Such an input was found to generate three output idlers, in agreement with theoretical predictions.

Our findings form solid ground for further exploration of the quantum properties of the NJPO field, which would exhibit four-mode squeezing and might possess non-Gaussian properties.

ACKNOWLEDGMENTS

We wish to express our gratitude to W. Wustmann, G. Ferrini, G. Johansson, and J. Burnett for helpful discussions. We also thank J. Aumentado for providing the shot-noise tunnel junction. We acknowledge financial support from the Knut and Alice Wallenberg Foundation and from the Swedish Research Council. J.B. acknowledges partial support from the EU under REA Grant Agreement No. CIG-618353.

- [1] R. J. Schoelkopf and S. M. Girvin, *Nature (London)* **451**, 664 (2008).
- [2] X. Gu, A. F. Kockum, A. Miranowicz, Y. X. Liu, and F. Nori, *Phys. Rep.* **718-719**, 1 (2017).
- [3] M. Hofheinz, H. Wang, M. Ansmann, R. C. Bialczak, E. Lucero, M. Neeley, A. D. O'Connell, D. Sank, J. Wenner, J. M. Martinis, and A. N. Cleland, *Nature (London)* **459**, 546 (2009).
- [4] C. Eichler, D. Bozyigit, C. Lang, M. Baur, L. Steffen, J. M. Fink, S. Filipp, and A. Wallraff, *Phys. Rev. Lett.* **107**, 113601 (2011).
- [5] E. Flurin, N. Roch, F. Mallet, M. H. Devoret, and B. Huard, *Phys. Rev. Lett.* **109**, 183901 (2012).
- [6] C. W. Chang, M. Simoen, J. Aumentado, C. Sabín, P. Forn-Díaz, A. M. Vadiraj, F. Quijandria, G. Johansson, I. Fuentes, and C. M. Wilson, *arXiv:1709.00083*.
- [7] B. Vlastakis, G. Kirchmair, Z. Leghtas, S. E. Nigg, L. Frunzio, S. M. Girvin, M. Mirrahimi, M. H. Devoret, and R. J. Schoelkopf, *Science* **342**, 607 (2013).
- [8] M. Sandberg, C. M. Wilson, F. Persson, T. Bauch, G. Johansson, V. Shumeiko, T. Duty, and P. Delsing, *Appl. Phys. Lett.* **92**, 203501 (2008).
- [9] T. Yamamoto, K. Inomata, M. Watanabe, K. Matsuba, T. Miyazaki, W. D. Oliver, Y. Nakamura, and J. Tsai, *Appl. Phys. Lett.* **93**, 042510 (2008).
- [10] M. Wallquist, V. S. Shumeiko, and G. Wendin, *Phys. Rev. B* **74**, 224506 (2006).
- [11] N. Bergeal, F. Schackert, M. Metcalfe, R. Vijay, V. E. Manucharyan, L. Frunzio, D. E. Prober, R. J. Schoelkopf, S. M. Girvin, and M. H. Devoret, *Nature (London)* **465**, 64 (2010).
- [12] C. M. Wilson, T. Duty, M. Sandberg, F. Persson, V. Shumeiko, and P. Delsing, *Phys. Rev. Lett.* **105**, 233907 (2010).
- [13] W. Wustmann and V. Shumeiko, *Phys. Rev. B* **87**, 184501 (2013).
- [14] C. H. Meaney, H. Nha, T. Duty, and G. J. Milburn, *EPJ Quantum Technol.* **1**, 7 (2014).
- [15] T. Inagaki, K. Inaba, R. Hamerly, K. Inoue, Y. Yamamoto, and H. Takesue, *Nat. Photonics* **10**, 415 (2016).

- [16] S. Puri, S. Boutin, and A. Blais, [npj Quantum Inf.](#) **3**, 18 (2017).
- [17] N. Bartolo, F. Minganti, W. Casteels, and C. Ciuti, [Phys. Rev. A](#) **94**, 033841 (2016).
- [18] M. Mirrahimi, Z. Leghtas, V. V. Albert, S. Touzard, R. J. Schoelkopf, L. Jiang, and M. H. Devoret, [New J. Phys.](#) **16**, 045014 (2014).
- [19] Z. R. Lin, K. Inomata, K. Koshino, W. D. Oliver, Y. Nakamura, J.-S. Tsai, and T. Yamamoto, [Nat. Commun.](#) **5**, 4480 (2014).
- [20] P. Krantz, A. Bengtsson, M. Simoen, S. Gustavsson, V. Shumeiko, W. D. Oliver, C. M. Wilson, P. Delsing, and J. Bylander, [Nat. Commun.](#) **7**, 11417 (2016).
- [21] W. Wustmann and V. Shumeiko, [Phys. Rev. Appl.](#) **8**, 024018 (2017).
- [22] M. Simoen, C. W. S. Chang, P. Krantz, J. Bylander, W. Wustmann, V. Shumeiko, P. Delsing, and C. M. Wilson, [J. Appl. Phys.](#) **118**, 154501 (2015).
- [23] E. Zakka-Bajjani, F. Nguyen, M. Lee, L. R. Vale, R. W. Simmonds, and J. Aumentado, [Nat. Phys.](#) **7**, 599 (2011).
- [24] B. Abdo, K. Sliwa, F. Schackert, N. Bergeal, M. Hatridge, L. Frunzio, A. D. Stone, and M. Devoret, [Phys. Rev. Lett.](#) **110**, 173902 (2013).
- [25] A. Heidmann, R. J. Horowicz, S. Reynaud, E. Giacobino, C. Fabre, and G. Camy, [Phys. Rev. Lett.](#) **59**, 2555 (1987).
- [26] R. Graham and H. Haken, [Z. Phys.](#) **210**, 276 (1968).
- [27] K. J. McNeil and C. W. Gardiner, [Phys. Rev. A](#) **28**, 1560 (1983).
- [28] S. Reynaud, [Europhys. Lett.](#) **4**, 427 (1987).
- [29] A. S. Lane, M. D. Reid, and D. F. Walls, [Phys. Rev. A](#) **38**, 788 (1988).
- [30] C. Fabre, E. Giacobino, A. Heidmann, and S. Reynaud, [J. Phys. \(Paris\)](#) **50**, 1209 (1989).
- [31] G. Björk and Y. Yamamoto, [Phys. Rev. A](#) **37**, 1991 (1988).
- [32] M. D. Reid and P. D. Drummond, [Phys. Rev. A](#) **40**, 4493 (1989).
- [33] J. Y. Courtois, A. Smith, C. Fabre, and S. Reynaud, [J. Mod. Opt.](#) **38**, 177 (1991).
- [34] F. Sun, X. Dong, J. Zou, M. I. Dykman, and H. B. Chan, [Nat. Commun.](#) **7**, 12694 (2016).
- [35] L. Spietz, K. W. Lehnert, I. Siddiqi, and R. J. Schoelkopf, [Science](#) **300**, 1929 (2003).
- [36] R. H. Koch, J. Clarke, W. M. Goubau, J. M. Martinis, C. M. Pegrum, and D. J. Van Harlingen, [J. Low Temp. Phys.](#) **51**, 207 (1983).
- [37] R. Adler, [Proc. IRE](#) **34**, 351 (1946).
- [38] J. Jing, S. Feng, R. Bloomer, and O. Pfister, [Phys. Rev. A](#) **74**, 041804 (2006).
- [39] A. Pikovsky, M. Rosenblum, and J. Kurths, *Synchronization: A Universal Concept in Nonlinear Sciences*, Cambridge Nonlinear Science Series Vol. 12 (Cambridge University Press, Cambridge, 2003).